Electrochimica Acta 570 (2026) 148958

Contents lists available at ScienceDirect

Electrochimica Acta

journal homepage: www.journals.elsevier.com/electrochimica-acta

One-step electrochemical synthesis of earth-abundant multi-metal-ion–doped polyaniline films for OER electrocatalysis

Arbnora Haljiti [a,1], Laís Gimenes Vernasqui [a,b,1,*], Bruna Ferreira Gomes [a,1,*], Lu Xia [c], Wulyu Jiang [c], Kaiqi Zhao [c], Tengyu Chen [c], Suelem Soares dos Santos [a,b], Philipp Hawe [a], F. Pelayo García de Arquer [c], Evaldo José Corat [b], Christina Roth [a]

[a] Electrochemical Process Engineering, University of Bayreuth, Universitätsstraße 30, Bayreuth 95447, Germany
[b] National Institute for Space Research – INPE, São José dos Campos, 12227-010, Brazil
[c] ICFO – Institut de Ciències Fotòniques, The Barcelona Institute of Science and Technology, 08860 Castelldefels, Barcelona, Spain

ARTICLE INFO

Keywords:
Polyaniline
Transition-metal-ion-doped conducting polymers
Multi-metallic electrocatalysts
Metal–nitrogen coordination
X-ray absorption spectroscopy (XAS)
^{15}N solid-state NMR
Oxygen evolution reaction (OER)

ABSTRACT

Nitrogen-rich conducting polymers such as polyaniline offer a tunable scaffold for earth-abundant oxygen evolution reaction (OER) sites, but progress is slowed by two challenges: i) multi-metal incorporation is typically achieved by post-doping, giving poorly defined stoichiometry and coordination, and ii) trace Fe in alkaline electrolytes can dominate the apparent activity of Ni-based motifs. Here we report a one-step cyclic-voltammetry co-deposition strategy that electropolymerizes aniline while embedding Fe, Ni and Mn ions into polyaniline (PAni), enabling mono-, bi- and trimetallic films without post-doping. Films are grown on carbon paper to remove substrate-derived activity and isolate composition–structure–performance correlations. Element-specific X-ray absorption spectroscopy (XAS; Fe/Ni/Mn K-edges) confirms ion uptake and competitive incorporation during mixed-ion growth, with a pronounced tendency toward Ni uptake (fluorescence intensity up to ~0.25 a.u. for PAni–Ni versus ~0.02 and ~0.01 a.u. for PAni–Mn and PAni–Fe, respectively), reflecting composition-dependent differences in the local metal coordination. Using ^{15}N-labeled PAni, solid-state ^{15}N NMR (CP-MAS and spin-echo) provides direct fingerprints of metal-nitrogen coupling beyond the sensitivity of extended X-ray absorption fine structure (EXAFS), distinguishing a distinct, strongly coupled N–Ni population from weaker Mn–N interactions and moderately coupled Fe–N environments. Crucially, OER testing in non-purified versus purified KOH decouples intrinsic activity from impurity-driven promotion: trace Fe increases the apparent activity of Ni-containing films, whereas only PAni–FeNiMn retains high activity under purified conditions, reaching an overpotential of 350 mV at 10 mA cm^{-2}. Together, these results show that multi-ion co-deposition leads to a balanced coordination regime that survives rigorous impurity control, establishing PAni as a structurally tailorable, low-loading platform for enhanced OER catalysis.

1. Introduction

Conductive polymers have attracted sustained interest as functional materials for electrochemical energy technologies due to their tunable electrical conductivity, structural adaptability, and intrinsic redox activity [1–6]. Among them, polyaniline (PAni) occupies a prominent position owing to its low synthesis cost, chemical stability, and the coexistence of multiple accessible oxidation states [7]. These features have enabled PAni to be widely explored in diverse applications, including supercapacitors [3,5], anticorrosion coatings [6], gas sensing [4], and energy-storage systems such as Li-ion, Zn-ion [1], and lead–acid batteries [8]. In these contexts, PAni frequently fulfills multiple roles simultaneously, acting as a conductive scaffold, a redox-active component, and a stabilizing medium for interfacial charge-transfer processes.

Beyond its intrinsic electrochemical functionality, PAni offers a chemically versatile backbone rich in amine and imine nitrogen sites capable of coordinating transition-metal ions (TMIs) [9]. This coordination ability enables the formation of hybrid polymer–metal systems in which metal centers can be uniformly distributed within the polymer matrix, often at very low metal loadings. Such architectures are

* Corresponding authors.
E-mail addresses: lais.vernasqui@inpe.br (L. Gimenes Vernasqui), bruna.lobo@uni-bayreuth.de (B. Ferreira Gomes).
[1] Those authors contributed equally.

https://doi.org/10.1016/j.electacta.2026.148958
Received 7 February 2026; Received in revised form 19 March 2026; Accepted 26 April 2026
Available online 27 April 2026

particularly attractive for electrocatalysis, as they maximize metal utilization while preserving electronic conductivity. However, conventional PAni–TMI composites are predominantly prepared via chemical polymerization followed by post-synthetic metal doping, typically involving ion exchange between protonic dopants and metal cations. While this approach has demonstrated promising catalytic effects—for instance, Pb-modified PAni improving HER behavior in lead–acid batteries [8]—it inherently limits control over metal dispersion, coordination environment, and metal–metal interactions.

Despite growing interest in PAni-based electrocatalysts, multimetallic PAni systems remain remarkably underexplored, particularly from a mechanistic and structural standpoint. To date, no reports describe an electrochemical one-step synthesis that simultaneously incorporates two or three different metal ions into PAni during polymer growth. This gap has significantly hindered systematic investigations of cooperative or competitive effects between different TMIs embedded within a conductive polymer framework. Moreover, metal–PAni coordination is intrinsically complex and highly sensitive to the nature of the metal ion, its oxidation state, and the local chemical environment. As a result, the existing literature rarely provides comprehensive and unambiguous structural characterization, especially using element-specific techniques capable of directly probing metal speciation, coordination geometry, and electronic interactions within the polymer matrix.

Addressing these limitations requires not only new synthesis strategies but also correlative, multi-technique characterization approaches capable of disentangling metal–metal, metal–nitrogen, and polymer-electronic effects. In this context, the present work fills a critical gap by introducing a one-step electrochemical co-deposition method that enables the controlled incorporation of Fe, Ni, and Mn into PAni, yielding mono-, bi-, and trimetallic films specifically designed for oxygen evolution reaction (OER) electrocatalysis. This electrochemical approach eliminates post-doping steps, accelerates film fabrication, and enables access to compositional combinations that are difficult to achieve via conventional routes, thereby significantly expanding the design space of PAni-based hybrid electrocatalysts [9].

More broadly, OER electrocatalysis has traditionally relied on noble-metal catalysts such as RuO_2 and IrO_2, as well as transition-metal oxides and hydroxides based on Ni, Fe, and Co, which represent the current benchmarks for activity in alkaline media [10,11]. Nevertheless, these systems often face limitations related to cost, metal utilization, and limited tunability of the active-site environment [12,13]. In this context, conductive polymer frameworks provide an attractive alternative platform, as their chemically versatile backbones can host isolated or weakly interacting metal centers while simultaneously ensuring electronic conductivity and structural adaptability. Such hybrid architectures enable efficient metal utilization and offer unique opportunities to tailor metal coordination environments within a functional catalytic matrix [14,15].

To elucidate the structure–property relationships governing these materials, an extensive multiscale characterization strategy was employed. SEM and Raman spectroscopy were used to assess morphology and polymer-backbone evolution upon metal incorporation. X-ray photoelectron spectroscopy (XPS) provided insights into nitrogen speciation and metal–nitrogen coordination effects at the surface, while X-ray absorption spectroscopy (XAS) enabled element-specific interrogation of the metal centers, including confirmation of metal incorporation, and semi-qualitative assessment of metal distribution and competition effects in bi- and trimetallic systems. Complementarily, solid-state ^{15}N solid NMR spectroscopy was employed on PAni films synthesized from ^{15}N-labeled aniline to directly probe the local chemical and electronic environments of nitrogen sites within proton-doped Pani. This combined NMR approach provides unique sensitivity to metal–nitrogen interactions and proximity effects that cannot be unambiguously resolved by EXAFS or XPS alone.

From an application perspective, this study demonstrates that PAni-based materials doped with very low metal and polymer loadings can nonetheless achieve high OER activity. The resulting hybrid films exhibit features reminiscent of single-atom-like catalysts, with isolated or weakly interacting metal centers embedded within a conductive polymer matrix. Furthermore, this work presents the first systematic investigation of electrolyte-purification effects on the intrinsic OER activity of PAni–TMI electrocatalysts. While Fe impurities in alkaline electrolytes are well known to artificially enhance the OER performance of Ni- and Co-based oxides [16–19], their impact on conductive-polymer-based systems—where metal–polymer coordination can further amplify or mask impurity effects—has remained unexplored. Here, electrolyte purification was used as a mechanistic probe to clarify the role of Fe within the PAni matrix, rather than as a simple electrolyte-cleaning test.

2. Experimental

2.1. Chemicals

Aniline (≥99%, Sigma-Aldrich) was purified by triple distillation at 185 °C. For the metal-doping process, manganese (II) sulfate monohydrate ($MnSO_4·H_2O$, ACS/Reag. pH.Eur., VWR Chemicals), iron (II) sulfate heptahydrate ($FeSO_4·7H_2O$, ≥99%, Sigma-Aldrich), and nickel (II) sulfate heptahydrate ($NiSO_4·7H_2O$, ≥99%, Sigma-Aldrich) were used. The electrochemical polymerization and deposition of PAni were carried out in 1 mol L^{-1} H_2SO_4 prepared from analytical-grade sulfuric acid (≥95%, Sigma-Aldrich).

For electrochemical testing, the electrolyte was prepared using reagent-grade potassium hydroxide flakes (KOH, ≥85%, Sigma-Aldrich). Electrolyte purification was performed using nickel(II) nitrate hexahydrate ($Ni(NO_3)_2·6H_2O$, ≥98.5%, Sigma-Aldrich).

2.2. PAni–TMI catalysts synthesis

Carbon paper (gas diffusion layers, SGL-10AA) was employed as the initial substrate for XAS, XPS, Raman, and electrochemical characterization. Although not a conventional OER substrate, carbon paper was intentionally used to avoid Ni-mesh-derived contributions, allowing reliable spectroscopic and electrochemical analysis of Ni species incorporated into PAni.

For PAni deposition, an aniline concentration of 0.036 mol L^{-1} in 1 mol L^{-1} H_2SO_4 was used. For PAni–TMI samples, the metal salts were then introduced, and the solution was stirred for 15 min. To enable a direct comparison between the different PAni–TMI catalysts, the concentrations of aniline and acid were kept constant throughout all syntheses.

The concentration of the metal sulfates used are listed in Table 1. An initial total metal-salt concentration of 25 mmol L^{-1} was employed, however, based on the deposition behavior of the Fe-containing solutions, the metal loadings were subsequently adjusted to obtain uniform and reproducible film growth.

PAni-based electrodes were prepared by cyclic voltammetry using a

Table 1
Concentration of the metal sulfates used for synthesizing the different PAni-TMI catalysts.

Sample	Metal	Concentration / mmol L^{-1}
PAni-Fe	Fe	25
PAni-Ni	Ni	25
PAni-Mn	Mn	25
PAni-FeNi	Fe	5
	Ni	5
PAni-FeMn	Fe	5
	Mn	5
PAni-NiMn	Ni	12.5
	Mn	12.5
PAni-FeNiMn	Fe	5
	Ni	10
	Mn	10

one-step electrochemical polymerization and metal-doping procedure. All depositions were performed under constant stirring at 5 °C. A three-electrode configuration was employed, with the GDL as the working electrode (WE), a platinum wire as the counter electrode (CE), and an Ag/AgCl in saturated KCl as reference electrode (RE). The CV deposition consisted of 20 cycles between −0.2 and 1.0 V vs. Ag/AgCl, starting and ending at open-circuit potential. Following deposition, the electrodes were rinsed with Milli-Q water and dried in a vacuum oven at 60 °C for 15 min; this procedure was repeated twice. Each carbon paper was weighed before and after deposition in order to estimate the deposited mass. Each deposition used a freshly prepared aniline/metal-salt solution, as reuse of the same solution resulted in thinner films. Between experiments, the CE was thoroughly cleaned by rinsing and flame annealing in open air to remove any residual polyaniline deposits and prevent cross-contamination.

2.3. . PAni–TMI catalysts characterization

Scanning electron microscopy (SEM, Zeiss Ultra Plus) was used to examine the surface morphology before and after electrochemical testing. Images were acquired at low accelerating voltage (EHT = 3.0 kV) to minimize electron-beam-induced damage to the polymeric PAni-based films and to enhance surface sensitivity. No conductive coating was applied prior to imaging, as no charging effects were observed due to the intrinsic conductivity of the proton-doped PAni matrix and the conductive substrate. XAS was performed ex situ at beamline P65 (PETRA III, DESY, Hamburg) at the Fe, Ni, and Mn K-edges using fluorescence detector. A multi-element SDD detector was used to improve sensitivity. Metal foils were used to align the energy for the different edges. The softwares Bessy_47b and SimXLite, both developed by the beam scientists at beamline KMC-3 (BESSY II – Berlin), were used for the data processing and EXAFS fitting, respectively. The ranges used for the EXAFS fit were: k = [2.0; 10.5] $Å^{-1}$ and R = [1.0; 2.5] Å, k = [2.0; 10.5] $Å^{-1}$ and R = [1.0; 2.5] Å and k = [2.0; 10.25] $Å^{-1}$ and R = [1.0; 2.0] Å for Mn, Ni and Fe K-edges, respectively. The amplitude reduction factors (S_0^2) used for the fit were 0.65, 0.9 and 0.8 for Mn, Ni and Fe K-edges, respectively. The scattering paths were obtained using the FEFF8 software and the CIF files obtained from the Material Project website.

XPS measurements were conducted using a PHI 5000 VersaProbe III system with monochromatic Al Kα radiation to determine surface composition and oxidation states. Data treatment was performed in CasaXPS.

Raman spectroscopy (LabRAM HR800, 633 nm) was used to analyze the vibrational structure of the films. Spectra were collected between 480 and 1640 cm^{-1}.

For solid-state ^{15}N NMR analysis, PAni and PAni–TMI samples were synthesized using ^{15}N-labeled aniline as the nitrogen source. Electrodeposition was carried out under the same electrochemical conditions employed for the unlabeled materials, maintaining identical acid-to-aniline ratios and metal precursor concentrations. A glassy carbon plate (exposed geometric area of approximately 4.5 cm^2) was used as the WE to enable the deposition of larger material quantities. To obtain sufficient material for NMR measurements, the number of potentiodynamic deposition cycles was increased to 120, promoting the growth of a thick PAni-based film that partially detached from the glassy carbon substrate during deposition. After synthesis, the deposited material was collected, vacuum-filtered, and subsequently dried under vacuum at 60 °C for 30 min prior to further characterization.

The samples were measured with our spectrometer Bruker Avance III 400 (Magnetic Field 9.4 T). ^{15}N CP MAS spectra were obtained using a ramped cross-polarization experiment, where the nutation frequency n_{nut} on the proton channel varied linearly by 30%. The samples were spun at 10.0 kHz in a 1.9 mm MAS triple resonance probe (Bruker). The corresponding n_{nut} on the ^{15}N channel and the contact time were adjusted to 66 kHz and 5 ms respectively. During acquisition proton broadband decoupling was applied using a spinal-64 sequence with n_{nut} = 90 kHz.

For the ^{15}N spin echo measurements we used the same probe head. The MAS speed was set to 25 kHz, the recycle delay to 50 ms and the ^{15}N 90° pulse length to 3.0 µs. ^{15}N spectra are referenced with respect to saturated NH_4NO_3 solution using the secondary standard glycine (σ(iso) = 11.59 ppm).

2.4. Electrochemical performance in half-cell setup

The OER electrochemical measurements were performed in 1 mol L^{-1} KOH using a three-electrode configuration with the PAni-based film as the WE, a Pt wire as counter electrode, and a Hydrogen Reference Electrode (HydroFlex, Gaskatel). The uncompensated solution resistance was partially corrected by 80% iR compensation using the current interrupt method, resulting in a residual resistance of approximately 5 Ω. The electrochemical cell had an electrolyte volume of 20 mL.

For the tests with purified KOH, a Ni-precipitation protocol was used [20]. In a 50 mL centrifuge tube, 2 g of $Ni(NO_3)_2{\cdot}6H_2O$ were dissolved in 4 mL of Milli-Q water, after which 20 mL of KOH were added to form the precipitate. The mixture was centrifuged for 2 min at 4000 rpm, and the supernatant was discarded. The precipitate was then washed by adding 20 mL of Milli-Q water and 2 mL of KOH, followed by centrifugation (2 min, 4000 rpm). This washing step was repeated three times. After the final wash, 45 mL of KOH were added, and the mixture was vigorously mixed and left to stand for at least 3 h before a final centrifugation (5 min, 4000 rpm). The purified KOH was filtered, and the resulting Ni-containing precipitate could be reused for up to four purification cycles.

To electrochemically characterize the electrodes regarding their OER activity, preconditioning was made before the CV applied to assess the OER performance. For the preconditioning, the electrodes were held at open-circuit potential (OCP) for 5 min, followed by 50 CV cycles between 0.4 and 1.6 V vs. RHE at 100 mV s^{-1}. For the obtained CVs, the maximum current density of the catalysts as well as the onset of OER is compared. The overpotential (η) was calculated by subtracting the thermodynamic potential at 10 mA cm^{-2} for OER (1.23 V vs. RHE).

3. Results and discussion

3.1. Metal–Dependent growth and incorporation in PAni–TMI systems

Fig. 1 shows the cyclic voltammograms recorded during the electrodeposition of PAni (Fig. 1a) and PAni–TMI composites (Fig. 1b–d) on GDL. For each material, two depositions are shown as solid and dashed curves, illustrating the reproducibility of the potentiodynamic polymerization method. The insets display the first deposition cycle for each sample, with red arrows marking the open-circuit potential (OCP) from which film growth was initiated.

From the inset of Fig. 1a, it becomes clear that the initial deposition cycle follows the characteristic behavior reported in the literature for PAni electropolymerization [21]. At the beginning of the anodic scan, no redox features associated with PAni are observed, as the system is dominated by the oxidation of the aniline monomer. Upon reversing the scan toward the cathodic direction, the first discernible redox response of PAni emerges. This behavior is further confirmed by the appearance of two well-defined oxidation peaks in the anodic region toward the end of the cycle, indicating the onset of polymer chain formation and the adhesion of the growing PAni film to the electrode surface.

From the increasing current densities observed over successive cycles in Fig. 1a, it becomes evident that the voltammetric profiles progressively evolve toward the characteristic redox behavior of conductive PAni [21,22]. The anodic features labelled A, B, and C correspond to the well-known transitions of the polymer: A reflects the oxidation of reduced PAni domains toward the emeraldine state; B is associated with the formation of quinoid (benzoquinone-type) structures; and C, at higher potentials, represents the conversion of emeraldine into the fully

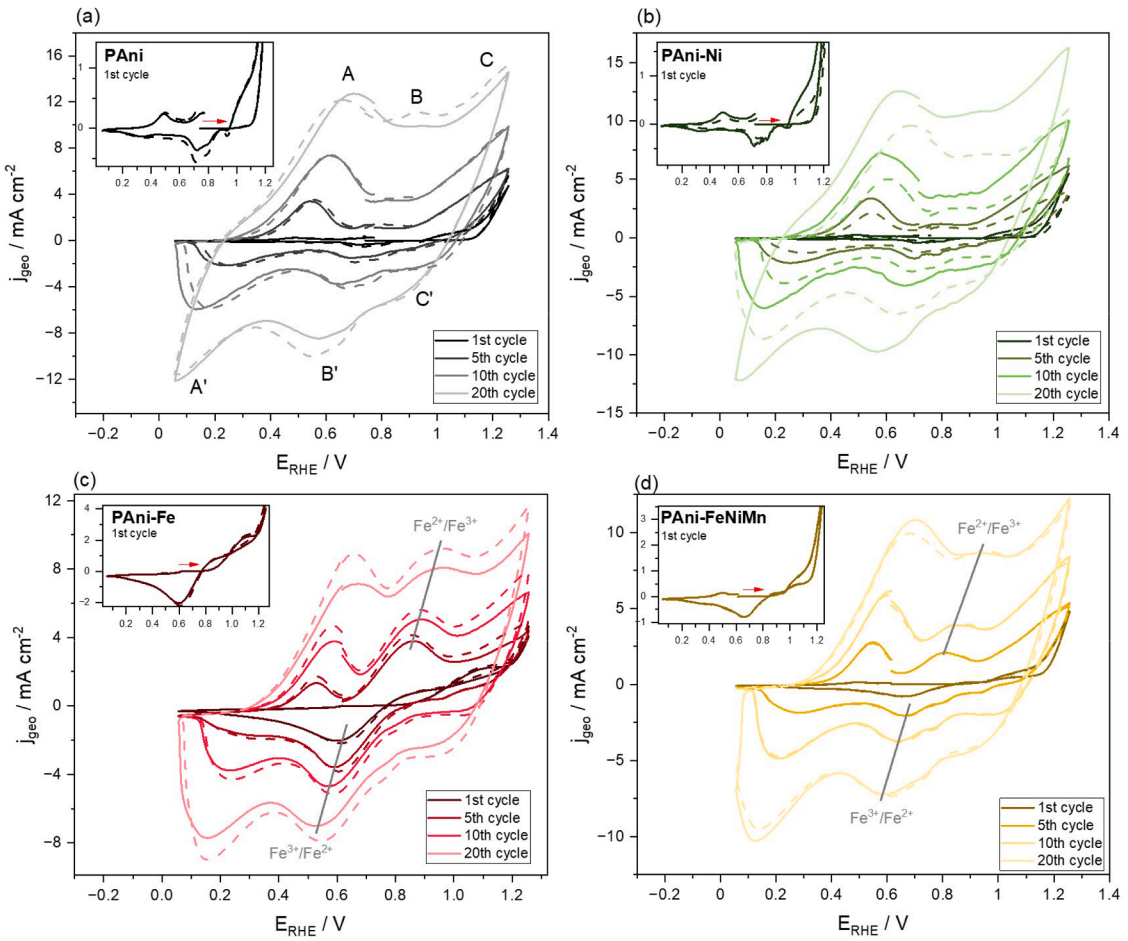

Fig. 1. Cyclic voltammograms recorded during the potentiodynamic deposition of (a) PAni, (b) PAni–Ni, (c) PAni–Fe and (d) PAni–FeNiMn. Dashed lines correspond to duplicate measurements, illustrating the reproducibility of the deposition process.

oxidized pernigraniline form. Each anodic transition is accompanied by a corresponding reduction peak in the reverse scan, consistent with the quasi-reversible redox behavior typical of PAni. As the deposition proceeds, peak A (~0.55 V vs RHE in the 5th cycle) increases in intensity. This behavior is expected, as peak A encompasses not only the emeraldine-forming transition but also the oxidation of aniline dimers into dimer cation-radicals—key intermediates required to sustain the polymerization process. In the fifth cycle, these two contributions become superimposed, as commonly reported in the literature [22]. Furthermore, the progressive shift of peak A toward higher potentials can be directly correlated with the increasing thickness of the PAni layer [23]. As the film grows, mass-transfer limitations become more pronounced due to the reduced availability of monomeric species at the electrode interface, requiring a higher overpotential to drive the same oxidation processes. This trend is also consistent with the autocatalytic nature of PAni polymerization reported in the literature, whereby the presence of an initial PAni layer accelerates further growth of the polymer. Once the first nuclei are formed, subsequent deposition becomes self-catalyzed, promoting faster chain propagation and film growth [22].

The deposition profiles of PAni–Ni (used as example in Fig. 1b), PAni–Mn and PAni–NiMn (Fig. S 1) show no significant deviations from the voltammetric behavior of the metal-free PAni. The presence of Ni^{2+}, Mn^{4+} or mixed ions does not introduce additional redox features nor does it alter the shape of the cyclic voltammograms. This similarity arises because, within the potential window used for the electropolymerization, the dominant process remains the oxidation of aniline. The metal ions do not undergo redox transitions in this region, Ni^{2+}/Ni^{3+} and Mn^{2+}/Mn^{3+} oxidations occur only at substantially higher potentials [24] and are therefore incorporated passively into the growing PAni matrix through coordination to amine/imine sites rather than through electrochemical conversion.

When iron is introduced during PAni deposition, either as the sole metal precursor, as shown in Fig. 1c, or in combination with Mn and Ni, as illustrated for PAni-FeNiMn in Fig. S 1, the voltammetric profile changes already from the first deposition cycle. In contrast to the behavior observed for PAni and for PAni–TMI systems containing, Ni^{2+}, Mn^{2+}, or both, the presence of Fe^{2+} modifies the shape and relative intensities of the redox features associated with aniline oxidation and early polymer growth. This behavior is likely related to the Fe^{2+}/Fe^{3+} redox couple, which occurs at approximately 0.77 V vs RHE, i.e., within the same potential window used for PAni electropolymerization [25]. Because this redox transition overlaps with the potential region where aniline is oxidized to form radical cations, the iron species can engage in competing electron-transfer processes, altering the concentration of reactive intermediates and thereby perturbing the polymerization pathway. Consequently, Fe^{2+} can disrupt the balance between monomer oxidation, radical coupling, and oligomer adsorption, leading to the distinct deposition pattern observed for the Fe-containing systems. It is important to note that the influence of iron on the voltammetric profile is less pronounced in the bi- and trimetallic systems. This may be linked to the iron concentration in those samples. As shown in Table 1, the Fe^{2+} concentration was substantially reduced in those samples compared to the monometallic PAni–Fe (from 25 mmol L^{-1} to 5 mmol L^{-1}). In the trimetallic composition, Fe is further diluted in the presence of higher concentrations of Ni^{2+} and Mn^{2+}.

The mass-loading results further support the electrochemical observations (Table S 1). The monometallic PAni–Fe sample exhibits the lowest film loading (0.403 mg cm^{-2}), reinforcing the conclusion that Fe species actively interfere with the polymerization process. In contrast, the incorporation of Ni (0.773 mg cm^{-2}) or NiMn (0.710 mg cm^{-2}) results in loadings comparable to pure PAni (0.873 mg cm^{-2}), indicating that these ions do not hinder the propagation of the polymer chains.

Having established the distinct electrochemical behaviors observed during PAni and PAni–TMI deposition, SEM analysis was conducted to evaluate how these differences translate into morphological changes in the resulting films. Fig. 2 presents representative micrographs of the bare GDL substrate, metal-free PAni, PAni–Fe and Pani–Ni, while SEM images of all mono, bi- and trimetallic catalysts are provided in Figs. S 2 and S 3.

The bare GDL displays the typical architecture of a carbon-fiber paper, consisting of thin, relatively smooth fibers randomly intertwined with no preferential orientation. At higher magnification, flake-like structures can be observed bridging the fibers, alongside visible voids and open channels, confirming the intrinsically porous nature of the substrate. Following PAni deposition, this fibrous network becomes almost entirely covered by a dense and continuous polymeric layer. The PAni film exhibits a finely textured and roughened morphology, which appears more pronounced at higher magnification. Compared to the bare GDL, the polymer layer is thicker, more porous, and forms a uniform coating that spans the fiber network with only a few residual open regions. These observations confirm that the one-step electropolymerization method enables the formation of homogeneous and well-adhered PAni films across the entire substrate.

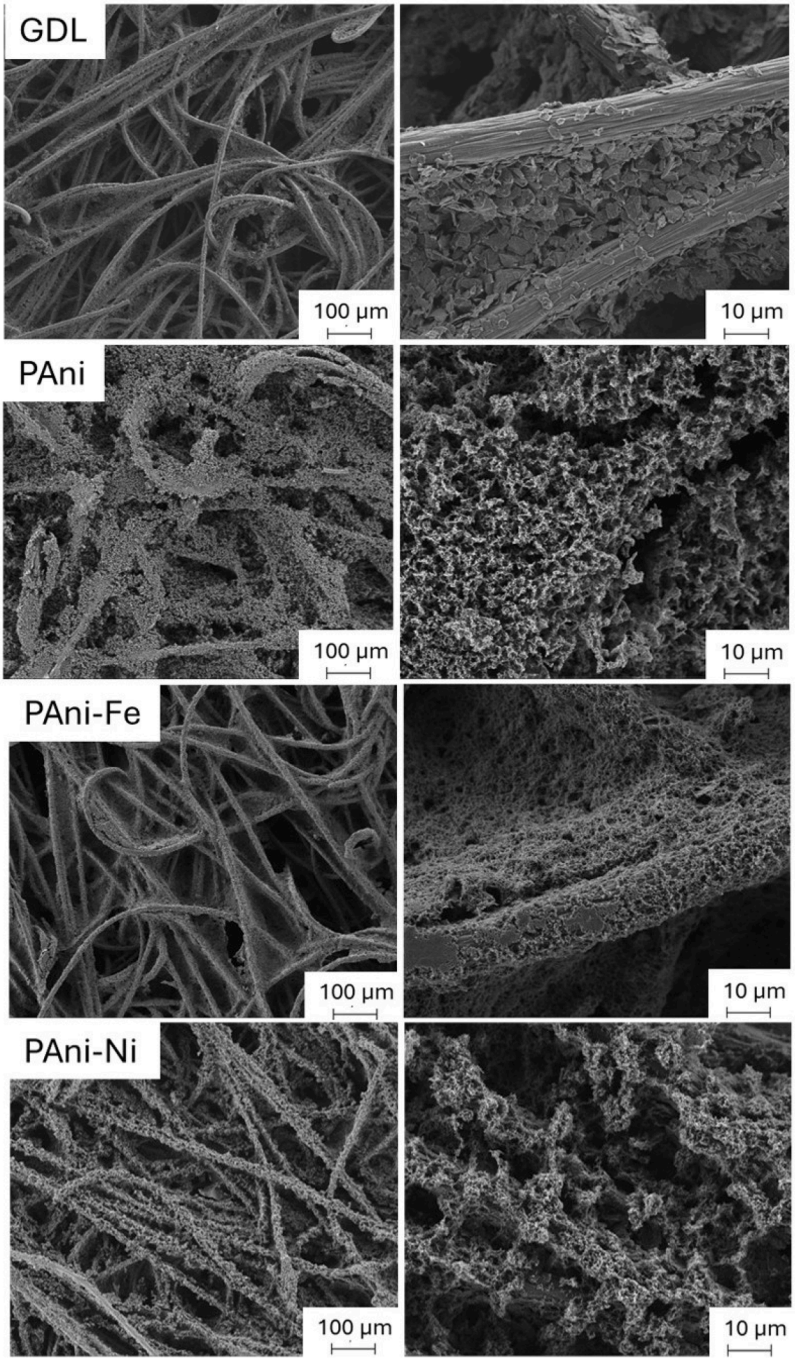

Fig. 2. SEM micrographs of the bare GDL substrate, PAni deposited on GDL, PAni–Fe and PAni-Ni, shown at both low (left)- and high magnification (right).

PAni–Fe was selected as an illustrative example of the metal-containing catalysts because it exhibited the lowest mass loading among all samples, allowing the assessment of film formation under the most conservative conditions. Despite the reduced amount of deposited material, the SEM images reveal excellent coverage of the carbon fibers, with the polymer uniformly distributed along the substrate surface. Although inter-fiber filling appears less pronounced compared to metal-free PAni, the coating remains cohesive and continuous. This behavior aligns with the electrochemical results where it is visible that the voltammetric profiles progressively converge toward the characteristic PAni pattern in the later cycles. In contrast, PAni–Ni, which displays a mass loading comparable to that of metal-free PAni, exhibits a very similar morphology, as shown in the corresponding SEM images.

SEM micrographs for the remaining mono-, bi- and trimetallic catalysts (Figs. S 2 and S 3) reveal similar trends, with continuous fiber coverage, reinforcing the effectiveness of the proposed method in producing uniform PAni and PAni–TMI coatings.

XAS measurements were performed on freshly prepared PAni-based samples on carbon paper to avoid nickel-mesh-related contributions present in single-cell configurations. This approach ensures that the observed spectroscopic features arise exclusively from the metal–PAni interactions. The measurements were performed in fluorescence mode due to the low metal loading in the samples. Under these conditions, conventional techniques for direct metal quantification, such as Energy-Dispersive X-ray Spectroscopy (EDX) or XPS, approach their detection limits. Therefore, XAS fluorescence intensity prior to spectral normalization was also analyzed as a semi-quantitative indicator of relative metal incorporation across the different samples.

The normalized XANES spectra at the Mn, Ni, and Fe K-edges are shown in Fig. 3a-c. Across the investigated compositions, the Mn and Ni K-edge spectra display only minor variations, indicating limited changes in their average oxidation states upon mono-, bi-, and trimetallic incorporation into the PAni matrix. In contrast, more noticeable spectral variations are observed at the Fe K-edge.

It should be emphasized that the Fe K-edge data exhibit a higher noise level compared to Mn and Ni due to their lower loading, which limits the spectral resolution and affects the reliability of subtle edge position and shape changes. This behavior is attributed to the relatively low iron concentration in these samples, and therefore any inferred changes in Fe oxidation state must be interpreted with caution, as they may be partially influenced by signal distortion and reduced signal-to-noise ratio. Despite this limitation, iron is the element showing the

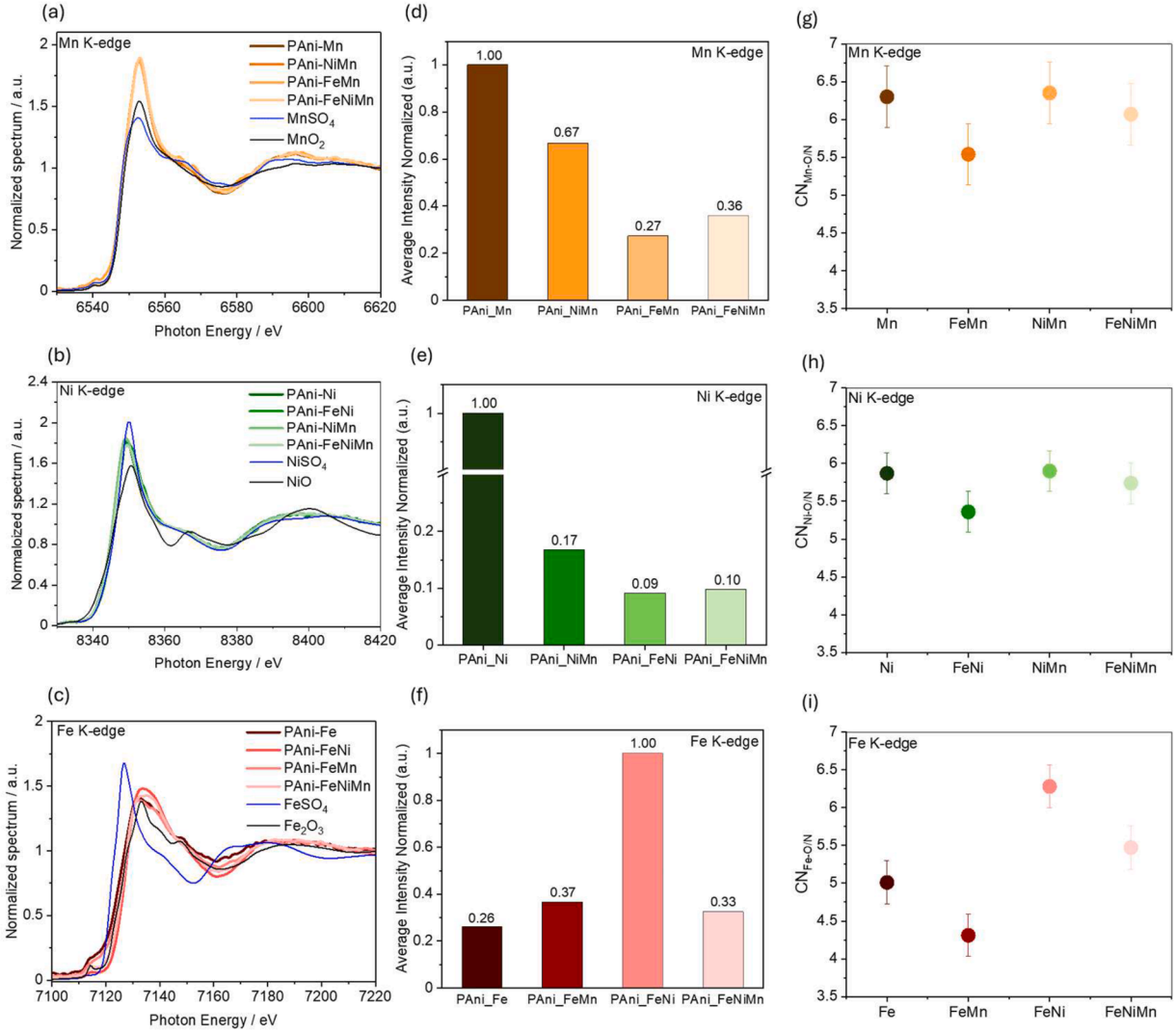

Fig. 3. Normalized XANES spectra at the (a) Mn K-edge, (b) Ni K-edge, and (c) Fe K-edge for the PAni-based samples. Panels (d), (e), and (f) present the average XANES intensities integrated over the energy windows 6950–6960 eV (Mn), 8750–8760 eV (Ni), and 7575–7585 eV (Fe). These intensities were extracted from background-subtracted XAS spectra prior to normalization and subsequently normalized to the maximum value within each series, allowing a relative comparison of metal ion incorporation in the PAni matrix. Panels (g), (h), and (i) display the coordination numbers extracted from EXAFS fitting at the Mn K-edge, Ni K-edge, and Fe K-edge, respectively. Error bars indicate the uncertainties associated with the EXAFS fitting parameters.

most pronounced variations among the three metals, suggesting a higher sensitivity of Fe ions to changes in the local chemical environment during co-deposition with PAni (Fig. 3a–c).

The oxidation states are primarily inferred from the edge position, typically evaluated from the maximum of the first derivative, while white-line intensity and post-edge features provide complementary information on the local coordination and electronic structure. For this reason, both the metal sulfate precursors and the corresponding oxide references were included for all analyzed metals, since counter-ions such as sulfate can influence spectral features and edge positions. A more detailed discussion of the oxidation states of the samples is provided in the Supporting Information accompanying Fig. S4.

In the case of Mn, the first-derivative maximum of the PAni–Mn sample coincides closely with that of MnO_2, supporting a predominant Mn^{4+} oxidation state (Fig. S 4). The substantially enhanced white-line intensity observed for Mn incorporated into the PAni matrix, compared to both the sulfate precursor and MnO_2, indicates a distinct local chemical environment, likely associated with Mn-polymer interactions. Importantly, this difference in spectral intensity does not contradict the Mn^{4+} assignment, as the oxidation state is dictated by the edge position rather than by white-line amplitude alone.

A similar behavior is observed for Fe, for which the XANES spectrum of Fe–PAni closely resembles that of Fe_2O_3, indicating the stabilization of Fe^{3+} species within the polymer matrix after synthesis [26]. Although Fe was introduced as $FeSO_4$, the absence of Fe^{2+}-like features suggests oxidation during or after co-deposition, consistent with the applied electrochemical window and with the thermodynamic tendency of Fe^{2+} to undergo oxidation to the more stable Fe^{3+} state under the synthesis conditions.

For Ni, the XANES spectrum shows a slightly modified edge shape and a reduced white-line intensity relative to the $NiSO_4$ precursor, while maintaining overall similarities in spectral features. This suggests a heterogeneous local environment, where Ni^{2+} species may coexist in different coordination motifs, including Ni–N coordination within the PAni backbone, residual sulfate-associated species, and possibly oxide-like environments.

XANES provides direct evidence that, after co-deposition, the metal species are stabilized within the PAni matrix in oxidation states corresponding to Mn^{4+}, Fe^{3+}, and Ni^{2+}, highlighting the strength of this technique in simultaneously probing oxidation states and local chemical environments in complex hybrid materials.

The differences in XANES signal intensity prior to normalization were exploited to obtain a semi-quantitative estimate of metal incorporation into the PAni matrix. The average intensities, extracted from background-subtracted but non-normalized XAS spectra and subsequently normalized to the maximum value within each series, are shown in Fig. 3d-f and summarized in Table S 3.

For Mn and Ni, the highest relative intensities are observed in the monometallic samples, indicating maximum metal uptake when no competing ions are present. In contrast, iron exhibits a distinct behavior, reaching its highest relative concentration when co-deposited with nickel and its lowest loading when deposited alone. This trend is consistent with deposition CVs and SEM observations, which indicate that iron deposited alone tends to oxidize more readily, leading to the formation of a thinner and mechanically weaker PAni film.

The trimetallic samples further highlight a direct competition among Mn, Ni, and Fe for active coordination sites within the PAni matrix during deposition. When considering the absolute fluorescence signal intensities (prior to normalization), nickel exhibits the highest incorporation when deposited alone, indicating a stronger overall affinity of Ni ions for coordination and stabilization within the PAni structure compared to Mn and Fe. For the monometallic samples, the maximum absolute fluorescence intensities reached approximately 0.01 a.u. for Fe, 0.02 a.u. for Mn, and 0.25 a.u. for Ni, respectively. Although Mn also shows enhanced incorporation in the monometallic system, its absolute signal intensity remains significantly lower than that of Ni.

The combined analysis of electrochemical deposition profiles, mass-loading data, SEM morphology, and XAS-derived incorporation trends provides a mechanistic framework to rationalize the formation of PAni–TMI catalysts during one-step electropolymerization. While Ni^{2+} and Mn^{4+} are incorporated largely passively, without significantly perturbing the polymerization pathway, Fe^{2+} introduces an additional redox process that overlaps with aniline oxidation. This leads to the competition between polymer growth and metal redox chemistry, thereby modulating growth kinetics, final loading, and metal uptake. As a result, precursor composition is not directly translated into the final PAni–TMI stoichiometry, highlighting a key design consideration for the synthesis of these hybrid catalysts.

3.2. Metal-Coordination environment in PAni–TMI systems

EXAFS fitting was performed using a single first-shell contribution (M–O/N). The k^3-weighted EXAFS spectra and corresponding magnitude of the Fourier-transformed EXAFS are presented in Fig. S 5 and the EXAFS fitting parameters are summarized in Table S 2. In addition to the limited data quality, a reliable distinction between nitrogen and oxygen backscattering paths is intrinsically challenging due to their similar atomic numbers and nearly identical scattering amplitudes and phases, as well as the very close M–N and M–O bond lengths. In addition, the structurally disordered nature of the polyaniline matrix likely results in mixed coordination environments and enhanced static disorder, further precluding a meaningful separation of individual M–N and M–O contributions. To avoid overparameterization and artificial correlations between coordination number (CN) and Debye–Waller factor, the σ^2 value was fixed to a common, physically reasonable value for all samples, allowing a meaningful relative comparison of coordination trends.

The extracted coordination numbers are presented in Fig. 3g-i. For Mn and Ni K-edges, only modest variations in CN are observed across the sample series, suggesting relatively stable average coordination environments. In contrast, the Fe K-edge exhibits significantly larger CN fluctuations, which is consistent with the dynamic behavior observed for iron during co-deposition in cyclic voltammetry experiments.

Interestingly, the FeMn and FeNi samples show the lowest coordination numbers at the Mn and Ni K-edges, respectively. This observation suggests that the presence of iron perturbs the local coordination geometry of Mn and Ni within the PAni matrix. For the trimetallic FeNiMn sample, a slight reduction in CN is observed compared to the corresponding monometallic systems, indicating competition between different metal ions for available coordination sites in PAni.

In contrast, iron reaches its highest coordination number (close to 6.0) when co-deposited with nickel, pointing to a stabilizing effect of Ni on Fe ions. This behavior suggests that Ni may facilitate the incorporation and stabilization of Fe within the PAni structure, promoting a more octahedral Fe coordination environment (Fig. 3d–f).

Solid-state ^{15}N NMR, combining CP-MAS and spin-echo experiments (Fig. 4), probes complementary subsets of nitrogen environments and provides a comprehensive and internally consistent picture of how Mn^{4+}, Fe^{3+}, and Ni^{2+} ions interact with proton-doped polyaniline (ranking Ni $\gg$ Fe $>$ Mn), resolving the nature and strength of metal–nitrogen interactions that cannot be unambiguously distinguished by EXAFS [27,28]. As all samples were synthesized electrochemically in 1 M H_2SO_4, the polymer is present in its emeraldine salt form, and protonic doping defines the baseline nitrogen environments.

In CP-MAS, magnetization is transferred from nearby ^1H nuclei to ^{15}N, making this technique particularly sensitive to protonated or proton-rich nitrogen sites and relatively rigid environments. As a result, CP-MAS preferentially highlights amine and protonated imine species in proton-doped polymers. In contrast, direct-excitation spin-echo experiments probe all ^{15}N nuclei irrespective of proton proximity but are highly sensitive to transverse relaxation effects. Nitrogen sites located near paramagnetic centers experience rapid T_2 relaxation and may therefore be strongly attenuated or completely suppressed in spin-echo

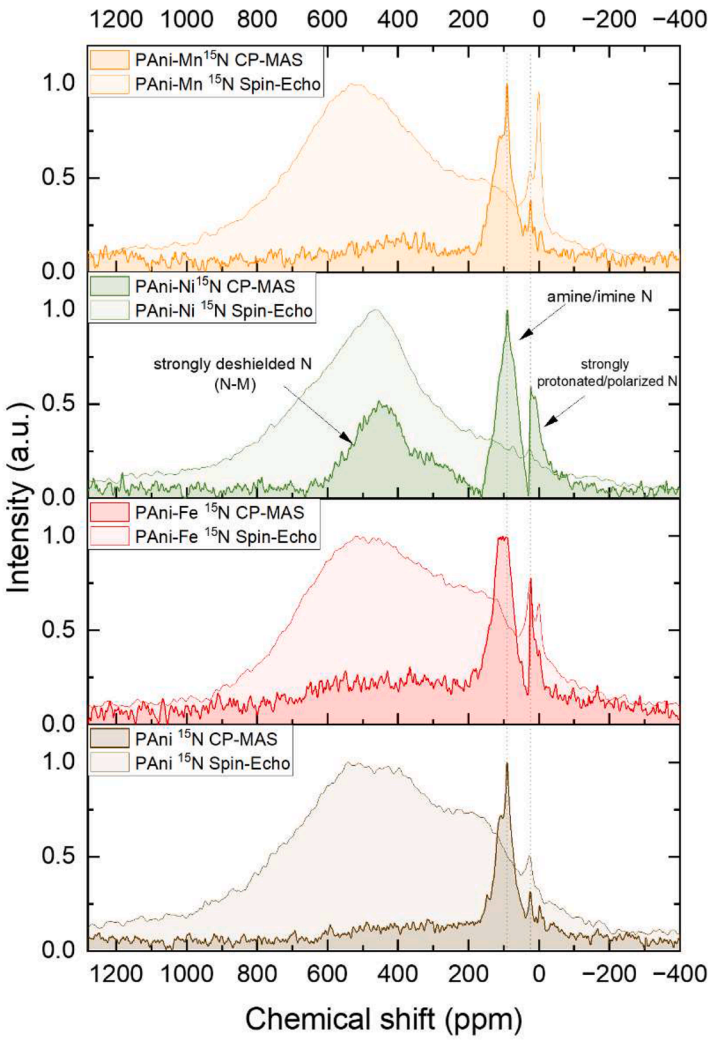

Fig. 4. Comparison of solid-state ^{15}N CP-MAS and spin-echo NMR spectra PAni and metal-containing PAni samples (Mn^{4+}, Ni^{2+} and Fe^{3+}). All spectra were acquired under identical experimental conditions optimized for PAni sample. CP-MAS spectra emphasize proton-proximal nitrogen environments, while spin-echo spectra probe all ^{15}N sites but selectively attenuate nuclei near paramagnetic centers due to rapid transverse relaxation.

spectra. Consequently, while CP-MAS emphasizes protonated nitrogen environments, spin-echo experiments provide enhanced sensitivity to metal–nitrogen proximity and paramagnetic interactions [28].

In the CP-MAS spectra of proton-doped PAni, the main resonance between ~50 and 150 ppm, with a maximum around 90 ppm and a shoulder near 107 ppm, reflects a distribution of amine (–NH–) and imine (=N–) nitrogen sites in different protonation states [29,30]. The signal at ~22–27 ppm is assigned to strongly protonated, polaronic or bipolaronic nitrogen species [31]. Upon metal incorporation, Fe^{3+} and Ni^{2+} induce a strong broadening of the amine/imine region, the disappearance of the imine-related shoulder, and a pronounced increase in the low-shift resonance, indicating a redistribution of nitrogen environments caused by metal–nitrogen interactions and partial modulation of protonic doping. In contrast, Mn^{4+} produces only minor changes in this region, suggesting preservation of the intrinsic proton-doped PAni backbone.

A key additional insight is provided by the high chemical shift region between ~200 and 600 ppm observed in CP-MAS. Proton-doped PAni exhibits only a weak, featureless contribution in this region, which represents the intrinsic background of the polymer [28]. Mn-containing PAni shows a comparable response, indicating that Mn^{4+} does not generate a significant population of strongly deshielded nitrogen sites. Fe-containing PAni displays a substantial increase in the integrated intensity of this region without a well-defined maximum, consistent with a heterogeneous distribution of Fe–N distances and moderately strong but spatially diverse metal–nitrogen interactions. Strikingly, Ni-containing PAni exhibits a clearly defined broad resonance in this region, with a maximum around 450 ppm and a shoulder near 300 ppm, revealing the presence of a distinct population of nitrogen sites [28] experiencing strong deshielding due to close electronic coupling with Ni^{2+}. Taken together, these nitrogen-specific NMR signatures provide compelling indirect evidence for strong and relatively homogeneous Ni–N interactions, thereby resolving the ligand ambiguity inherent to EXAFS alone.

Spin-echo measurements corroborate this interpretation by selectively suppressing nitrogen sites near paramagnetic centers. Proton-doped PAni exhibits an extremely broad envelope (~1000 to −200 ppm) with shoulders near ~600 and ~200 ppm and a narrow resonance at ~27 ppm, confirming the coexistence of distributed nitrogen environments and a small population of well-defined, strongly protonated sites. For Fe-containing PAni, the narrow low-shift resonances increase markedly in total area, indicating an enhanced population of strongly polarized nitrogen sites that remain sufficiently distant from Fe^{3+} centers to be observable. Notably, the spin-echo spectrum of Fe-containing PAni reveals a splitting of the low-shift resonance into two narrow components near ~26 ppm and ~1–2 ppm. Rather than indicating two well-defined crystallographic nitrogen sites, this behavior is more consistently interpreted as the presence of two distinct electronic

regimes of nitrogen polarization within the disordered polymer matrix. These two components likely correspond to strongly protonated nitrogen sites experiencing different degrees of electronic coupling to Fe^{3+} centers, reflecting variations in Fe–N proximity and local coordination geometry. In contrast, Ni-containing PAni shows a drastic attenuation of narrow resonances in spin-echo experiments, consistent with very rapid transverse relaxation of nitrogen nuclei located in close proximity to Ni^{2+}. For Mn-containing PAni, the persistence and growth of narrow low-shift resonances, together with minimal changes in CP-MAS, indicate that Mn^{4+} primarily redistributes protonic doping without forming a significant population of nitrogen sites in close electronic contact.

From a combined spectroscopic perspective, the XAS and ^{15}N NMR results demonstrate that, although all three metals are incorporated into the PAni matrix, they interact with the polymer nitrogen sites in fundamentally different ways. Taken together, these results demonstrate that the pronounced spectral changes induced by Fe^{3+} and Ni^{2+} arise from the interplay between paramagnetism and chemically specific metal–nitrogen interactions. While Fe^{3+} generates a broad distribution of N–Fe environments, Ni^{2+} forms a distinct population of strongly coupled N–Ni sites, clearly identifiable through the emergence of high-shift resonances in CP-MAS and their suppression in spin-echo experiments. Mn^{4+}, in contrast, remains largely decoupled from the nitrogen backbone, despite being present in the material, as confirmed by XAS.

In contrast to pyrolyzed PAni systems reported in the literature [28], where strong paramagnetic effects suppress CP-based experiments, the non-pyrolyzed and mildly doped PAni studied here allows the observation of ^{15}N signals in both CP-MAS and spin-echo experiments. The simultaneous visibility of signals indicates a moderate paramagnetic regime, in which variations in band intensity can be correlated with the strength of metal–nitrogen interactions. In this context, Ni-doped samples show the strongest perturbation, consistent with a stronger adsorption or coordination of Ni species to nitrogen sites.

Table 2 presents the summary of ^{15}N chemical shift regions and assignments discussed.

To probe the composition and further investigate the chemical environment of the incorporated metals and their influence on the polymer backbone, XPS analysis was employed. The survey spectra (Fig. S 6) confirm that all samples retain the expected elemental profile of PAni, with average surface compositions of approximately 74–77% C, 10–13% O, 7–10% N and 3–4% S. These values are fully consistent with the chemical structure of PAni deposited under acidic conditions, where residual sulfate and oxygen-containing surface groups are commonly detected [32]. For the PAni–TMI samples, the metal signals at the Fe 2p, Ni 2p and Mn 2p binding energies are not clearly observed in the survey spectra. This behavior arises from the growth of PAni as a textured and relatively thick layer under potentiodynamic conditions, in which the metal ions are homogeneously distributed within the polymer matrix instead of being surface-enriched, making their detection by XPS difficult. Nevertheless, this does not imply that the metal sites are electrochemically inaccessible, as PAni films typically form porous and electronically conductive networks (Figs. S 2, S 3) that allow electrolyte penetration and electrochemical access to metal centers distributed within the polymer framework [33].

While XPS survey spectra provide valuable confirmation of the expected PAni composition, detailed insights into metal incorporation can be extracted primarily from the N 1s region where coordination with the polymer backbone leaves characteristic fingerprints [34]. Fig. 5a-d presents the N 1 s core-level spectra for the PAni and PAni-TMI monometallic samples as example for PAni-TMI catalysts (the deconvolutions for all samples are presented in Fig. S 7). Although the metal signals are not directly detectable in the XPS survey spectra due to the low loadings and the distribution of the metals within the polymer matrix, metal incorporation can be inferred from the induced changes in the N 1s region, where metal–nitrogen coordination perturbs the local electronic environment and produces characteristic spectral shifts.

For PAni (Fig. 5a) the N 1s region exhibits the characteristic contributions assigned to imine (=N–), amine (–NH–), and the two protonated species (polaronic –NH•⁺– and iminium –N⁺=), in agreement with previous reports for emeraldine-type PAni formed under anodic conditions in acidic media [8,35]. A minor contribution at lower binding energy is attributed to N–O species [36]. The relative distribution dominated by imine (~55%), followed by amine (~21%) and polaronic/iminium nitrogen, matches closely the expected composition of emeraldine-base PAni partially protonated during synthesis in 1 mol L^{-1} H_2SO_4. A clear and consistent trend emerges for the monometallic PAni–TMI systems. When individual metal ions (Ni, Fe, or Mn) were incorporated into the PAni matrix, two main effects are systematically observed: (i) an apparent increase in the relative amine contribution and (ii) the disappearance of the iminium component for PAni-Ni and PAni-Fe. In contrast, the iminium contribution remains detectable for PAni–Mn suggesting that Mn perturbs the nitrogen speciation of PAni in a fundamentally different manner, as highlighted in the NMR analysis.

The increase in the amine-related contribution does not necessarily indicate a true chemical enrichment of benzenoid amine units in the polymer backbone. According to the literature, transition-metal ions preferentially coordinate to imine nitrogen sites in PAni, where lone-pair electrons are available for metal binding [37–39]. Such preferred coordination perturbs the local electronic density around the nitrogen atoms, leading to shifts in binding energy that are directly reflected in the N 1s spectra. In systems based on pyrolyzed or carbonized PAni–metal composites, this interaction is typically resolved as a distinct N–M contribution located between ~399 and 400 eV, widely reported as a fingerprint of M–N_x–C bonding environments [36,40]. In the present case, however, the PAni framework remains non-pyrolyzed, and the metal–nitrogen coordination contribution is not energetically separated from the intrinsic amine signal of the polymer [41]. As a consequence, the N–M contribution overlaps with the amine region and cannot be independently resolved by peak deconvolution. This overlap leads to an apparent increase in the amine fraction upon metal incorporation, even though this increase partially reflects the contribution of metal-coordinated nitrogen sites rather than a genuine growth of benzenoid amine species [34].

Table 2
Summary of ^{15}N chemical shift regions and assignments.

δ(^{15}N) / ppm	Technique(s)	Assigned nitrogen environment	Physical meaning / behavior
~90	CP-MAS	Amine N (–NH–), partially protonated	Dominant backbone N in proton-doped PAni
~107	CP-MAS	Imine N (=N–), weakly protonated	Shoulder in PAni; disappears upon Fe/Ni incorporation
50–180	CP-MAS	Distribution of perturbed amine/imine N	Broadens strongly for Fe^{3+} and Ni^{2+}, and slightly for Mn^{4+}, due to metal–N interactions
~22–27	CP-MAS & spin-echo	Strongly protonated N (polaronic/bipolaronic) and/or strongly polarized N	Area increases for Fe and Mn; strongly suppressed for Ni in spin-echo
~200–600	CP-MAS	Strongly deshielded N (N–M proximity, pseudocontact/contact shift)	Weak background in PAni/Mn; broad distribution for Fe; distinct N–Ni population for Ni
~600 / ~200 (shoulders)	spin-echo	Weakly protonated or electronically distinct N environments	Preserved in PAni and slightly changed for PAni–Mn/Fe; strongly altered for Ni
~1000 to −200	spin-echo	Full distribution of nitrogen environments	Reflects overall structural and electronic disorder

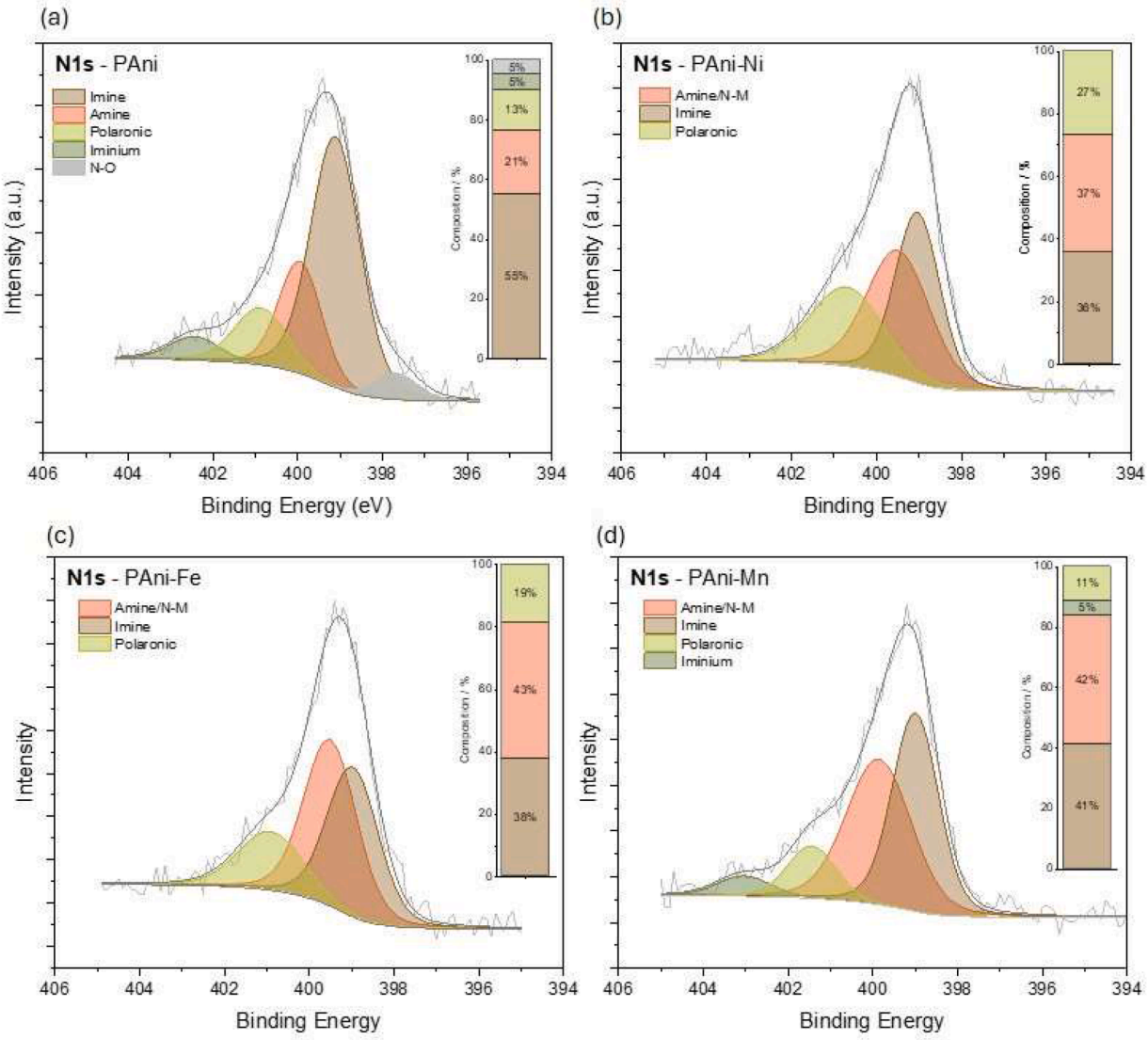

Fig. 5. High-resolution N 1s XPS spectra of (a) pristine PAni, (b) PAni–Ni, (c) PAni–Fe and (d) PAni–Mn electrodes. The experimental spectra (grey) were deconvoluted into contributions assigned to imine (=N–), amine (–NH–), polaronic nitrogen (–NH•⁺–), iminium nitrogen (–N⁺=), and minor N–O species when present. Bar charts summarize the relative surface composition of each nitrogen species, derived from the integrated peak areas.

In parallel, the disappearance of the iminium component upon metal incorporation (for PAni-Ni and PAni-Fe) provides further insight into the interaction between the transition metals and the PAni backbone. The iminium signal is associated with protonated imine sites and thus reflects the degree of protonic doping in the emeraldine salt form. Its suppression may indicate that imine nitrogen sites are no longer primarily stabilized by protonation but instead participate in coordination interactions with the metal ions. This interpretation is strongly supported by the ^{15}N solid-state NMR results, which reveal pronounced broadening, loss of imine-related features, and strong paramagnetic effects for Fe^{3+}- and Ni^{2+}-containing samples, consistent with close metal–nitrogen coupling.

The iminium presence observed for the Mn monometallic systems are also present for bi- and trimetallic systems (Fig. S 7) confirming that the presence of Mn perturbs the nitrogen speciation of PAni in a less pronounced manner compared to Ni- and Fe-only systems. In addition, an apparent increase in the amine contribution is also observed for the bi- and trimetallic samples, consistent with the overlap between intrinsic amine nitrogen and metal–nitrogen coordination features in the N 1s region.

Taken together, the combined XPS and NMR results demonstrate that the incorporation of transition metal ions into PAni leads to a reorganization of nitrogen functionalities, in which protonated iminium sites are progressively replaced by metal-coordinated nitrogen environments. This redistribution explains both the apparent increase in the amine fraction and the disappearance of the iminium component in XPS and underlines the conclusion that metal–nitrogen coordination plays a central role in defining the electronic structure of the PAni–TMI catalysts.

Raman spectroscopy (Fig. S 8) further corroborates the structural patterns discussed from XPS, confirming that metal ion incorporation does not disrupt the characteristic backbone of doped PAni but rather preserves its expected electronic structure. All samples exhibit the vibrational modes typical of emeraldine-type PAni, with bands at ~1589 cm^{-1} and ~1468 cm^{-1} assigned to C = C stretching of benzenoid units and C = N stretching of quinoid segments, respectively, alongside features at ~1217 cm^{-1} and ~1165 cm^{-1} related to C–N stretching and C–H vibrations in quinone or semiquinone structures [42]. Importantly, a weak but discernible band at ~1333 cm^{-1}, attributed to C–N•⁺ vibrations associated with polaronic segments in the emeraldine salt form, is observed for all samples, reinforcing the significant contribution of polaronic and protonated nitrogen species [42]. This observation further

supports the co-doped nature of the PAni matrix, in which protonic doping by the acidic medium is complemented by metal-induced electronic interactions, in agreement with the trends inferred from XAS, ^{15}N solid-state NMR and XPS analyses.

3.3. . Impurity overwrite principle

The oxygen evolution reaction (OER) in alkaline media is a kinetically demanding, four-electron process governed by the formation and stabilization of oxygenated intermediates (M–O and M–OOH) at the catalyst surface, making catalyst composition and electronic structure key parameters for activity [43,44]. The electrochemical performance of the PAni–TMI electrodes was evaluated by cyclic voltammetry, initially in non-purified KOH, to assess how metal incorporation into the polymer backbone influences OER activity. Fig. 6 displays only pristine PAni and the PAni–TMI compositions that exhibited a measurable OER response under the investigated conditions, while the voltammograms of the remaining samples are provided in the Fig. S 9.

From Fig. 6a, it is possible to observe a clear dependence of OER activity on the presence of Ni in the PAni matrix. While pristine PAni and most Fe- or Mn-only systems display negligible anodic currents (Fig. S 9) within the investigated potential window, Ni-containing electrodes exhibit pronounced OER activity. In particular, PAni–Ni, PAni–NiMn, and PAni–FeNiMn reach maximum current densities of approximately 167, 140, and 116 mA cm^{-2} at 1.8 V vs RHE, respectively. This strong correlation indicates that Ni incorporation is a prerequisite for activating the PAni-based electrodes toward OER under these conditions. Notably, this catalytic trend is consistent with the spectroscopic evidence obtained from ^{15}N solid-state NMR, XPS, and XAS, which collectively indicate a stronger interaction and preferential stabilization of Ni species within the PAni matrix compared to Fe and Mn. Such enhanced Ni-based motifs interaction likely facilitates the formation of catalytically active Ni-centered sites, thereby contributing to the observed increase in OER activity. To enable a more meaningful comparison between samples with different loadings, mass activities were calculated using the highest current density obtained for each composition. Based on this metric, PAni–Ni reaches a maximum mass activity of ~296 A g^{-1}, followed by PAni–NiMn (~214 A g^{-1}) and PAni–FeNiMn (~200 A g^{-1}). These values confirm that Ni-containing systems do not only deliver higher absolute currents but also outperform other compositions when normalized to the deposited mass (Table S 4).

To further compare the OER performance of the most active electrodes, the corresponding overpotential at 10 mA cm^{-2} were extracted for samples in non-purified KOH. Among all compositions, PAni–Ni consistently exhibits the lowest overpotential of approximately 0.29 V, indicating the most favorable OER kinetics within this series. The incorporation of additional metals leads to a systematic increase in overpotential, with PAni–FeNiMn and PAni–NiMn displaying 0.32 V of overpotential. PAni–FeMn shows the highest overpotential (~0.41 V), reflecting less efficient OER catalysis.

A direct comparison of these values with literature reports is not straightforward, as truly analogous systems are scarce. Most PAni-based OER catalysts reported to date rely on chemical polymerization routes, where PAni is post-doped with metal species [45–47], or involve the electrochemical or chemical/electrochemical deposition of PAni onto pre-formed metal oxide layers [48,49], rather than the one-step electrochemical incorporation of metal ions during polymer growth as employed here. Nevertheless, some relevant literature systems employ the nitrogen functionalities of PAni [45,49,50], particularly imine sites, as anchoring sites for Ni–Fe oxide or oxyhydroxide motifs. In such PAni-supported Ni–Fe-based OER catalysts, overpotentials typically reported at 10 mA cm^{-2} fall in the range of ~0.25 to 0.325 V in alkaline media [45,49,50].

Comparable overpotentials have also been reported for bimetallic PAni-based systems containing Ni and Co, where values between ~0.25 and 0.28 V are achieved without explicit purification of the alkaline electrolyte [46,47] . Within this context, the overpotentials observed here for PAni–Ni, PAni–NiMn, and PAni–FeNiMn in non-purified KOH (0.29–0.41 V) place the present materials well within the expected performance window for PAni-assisted Ni–Fe OER catalysts, despite their fundamentally different synthesis strategy and metal dispersion.

However, it is widely reported in the literature that trace Fe impurities in the electrolyte can dramatically enhance the apparent OER activity of Ni-based catalysts [16,17]. Under these conditions, Fe from the electrolyte can be incorporated into Ni active sites during operation, leading to the formation of highly active Ni–Fe motifs that modify the intrinsic catalytic behavior of the material [18]. Therefore, while the trends observed in non-purified electrolyte clearly identify Ni as the key activity-inducing element, they do not allow an unambiguous distinction between intrinsic activity and impurity-driven enhancement [19]. To decouple intrinsic catalytic activity from impurity-driven enhancement, the three best-performing catalysts (PAni-Ni, PAni–NiMn, and PAni–FeNiMn) were subsequently evaluated in purified KOH (Fig. 6b). This purification step acts as a mechanistic probe, selectively suppressing electrolyte-mediated Fe promotion and thereby exposing the stability of the underlying metal–PAni coordination framework.

Under purified conditions, a substantial decrease in current density is observed for some samples. In PAni-Ni and PAni-NiMn samples, both showed maximum current densities below 20 mA cm^{-2}, a decrease by up to 5 times. This behavior is consistent with literature reports describing

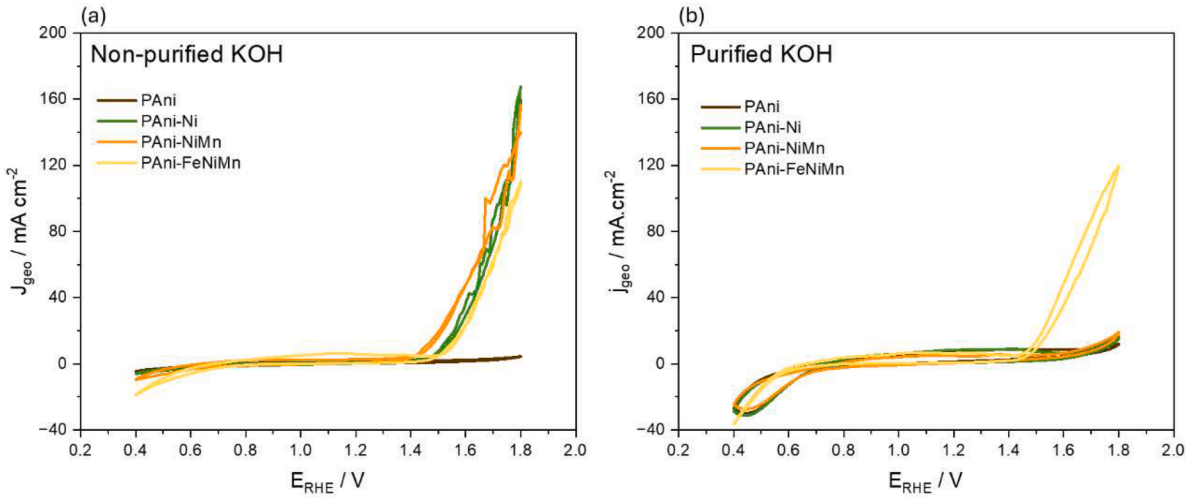

Fig. 6. CVs in 1 mol L^{-1} KOH from 0.4 to 1.8 V vs. RHE at 10 mV s^{-1} for PAni and PAni-TMI catalyst. (a) Non-purified and (b) purified electrolyte.

Fe-induced electronic modification of Ni sites, which facilitates the formation of catalytically active NiOOH species at lower potentials [16–19]. While such effects are most discussed for bulk Ni-based catalysts [51], the present results demonstrate that even at the level of isolated or polymer-coordinated metal centers, trace amounts of Fe play a decisive role in governing the observed OER activity.

Interestingly, PAni–FeNi exhibits negligible OER activity in non-purified KOH (Fig. S 9), even though Fe impurities are widely reported to enhance the activity of Ni-based catalysts. XANES results revealed that, in the presence of Fe, the relative incorporation of Ni into the PAni matrix is substantially reduced, while the Fe content increases markedly. This observation suggests that the beneficial effect of Fe on Ni-catalyzed OER is highly sensitive to its concentration and local coordination environment. These results indicate that only small amounts of Fe, such as trace impurities in non-purified KOH, are sufficient to electronically promote Ni sites and facilitate the formation of NiOOH species. When the Fe content exceeds a certain threshold, however, the catalytic performance deteriorates, likely due to dilution of active Ni sites and disruption of the optimal Ni electronic structure.

Of the four depositions tested, only PAni-FeNiMn shows any significant catalytic activity for OER, being comparable to the ones in non-purified KOH, reaching up to 120 mA cm^{-2}. The onset for OER is even better than the one observed without purification (0.32 V for non-purified KOH and 0.25 V for the purified KOH). This behavior can be rationalized by the more balanced incorporation of Fe and Ni revealed by XANES. In this system, Fe appears to act as an electronic promoter without fully suppressing the presence of catalytically active Ni sites. The polymeric PAni matrix likely accentuates this effect by spatially confining the metal centers, thereby making the system particularly sensitive to metal–metal competition and coordination chemistry.

To summarize, the contrasting behavior observed among the Ni-containing systems under purified conditions provides important mechanistic insight into the role of metal–polymer coordination balance. XANES analysis revealed that Fe incorporation strongly suppresses Ni uptake in the PAni matrix, while simultaneously increasing the relative Fe content. In the bimetallic PAni–FeNi system, this imbalance likely leads to a dilution or disruption of the population of Ni–N coordination sites that was identified by ^{15}N NMR as strongly coupled Ni–N motifs within the PAni matrix, which are proposed to stabilize Ni-centered species relevant for OER activity. As a consequence, despite the presence of Fe, the system fails to retain intrinsic OER activity once electrolyte-mediated Fe promotion is removed. In contrast, the trimetallic PAni–FeNiMn system maintains significant activity under purified conditions. This behavior may be explained by the weak and non-specific interaction of Mn with the PAni nitrogen backbone, as evidenced by both NMR and XPS, which allows Mn to act as a structural moderator rather than a direct active site. By perturbing the protonation and nitrogen population of PAni without strongly competing for coordination sites, Mn prevents complete displacement of Ni by Fe, thereby preserving a balanced distribution of metal-nitrogen interactions in which Fe acts as an electronic promoter while Ni–N motifs remain intact. This balance enables PAni–FeNiMn to sustain OER activity even in the absence of electrolyte-derived Fe impurities.

Besides, post-mortem SEM images (Fig. S 10) were acquired to assess potential morphological changes induced by electrochemical operation. The PAni and PAni-TMI electrodes largely retain their porous and interconnected morphology after OER testing, indicating good structural stability in alkaline media. No pronounced particle agglomeration or formation of dense catalyst domains is observed within the resolution of SEM, suggesting that the PAni matrix effectively preserves the electrode architecture during operation, avoiding structural degradation.

4. Conclusions

This work demonstrates a one-step electrochemical co-deposition strategy to incorporate Fe, Ni, and Mn ions into polyaniline (PAni) during polymer growth, enabling the synthesis of mono-, bi-, and trimetallic PAni films without post-doping. By coupling metal incorporation directly to the electropolymerization process, this method provides access to hybrid polymer–metal systems with controlled compositions and coordination environments that are difficult to achieve through conventional synthetic routes.

The combined spectroscopic analysis reveals that the incorporated metals interact with the PAni matrix in fundamentally different ways. While Ni forms a distinct population of strongly coupled Ni–N sites within the polymer backbone, Fe induces a broader distribution of Fe–N interactions, and Mn remains comparatively weakly coupled to the nitrogen framework. These differences highlight the key role of metal–polymer coordination in defining the local electronic structure of the PAni–TMI systems and demonstrate how competitive incorporation of multiple metals can modulate the coordination environment within the polymer matrix.

Electrochemical measurements further show that Ni incorporation is essential for activating PAni toward the oxygen evolution reaction, while the apparent activity of Ni-containing systems in non-purified electrolyte is strongly influenced by trace Fe impurities. When tested in purified electrolyte, only the trimetallic PAni–FeNiMn catalyst retains significant OER activity, indicating that a balanced metal incorporation and coordination environment is required to sustain intrinsic catalytic performance.

Overall, these findings demonstrate that electrochemical co-deposition provides a versatile platform for engineering polymer–metal hybrid electrocatalysts with tunable coordination environments. By combining spectroscopic insight with electrochemical analysis, this work highlights the importance of controlling both metal incorporation and electrolyte purity when evaluating conductive polymer–based OER catalysts and provides a framework for the rational design of low-loaded polymer-supported catalytic systems for electrochemical energy conversion.

Future studies will systematically address the optimization of the Ni/Fe ratio within the one-step co-deposition approach, aiming to establish correlations between synthesis parameters, metal incorporation, and catalytic performance. In addition, comprehensive investigations of catalyst stability and reaction kinetics under OER conditions will be conducted, including long-term electrochemical measurements, impedance analysis, and operando X-ray absorption spectroscopy (XAS) to resolve dynamic changes in the coordination environment of Ni within the PAni matrix during catalysis.

Declaration of competing interest

The authors declare the following financial interests/personal relationships which may be considered as potential competing interests:

Bruna Ferreira Gomes reports financial support was provided by Federal Ministry of Research, Technology and Space and Space. Philipp Hawe reports financial support was provided by Deutsche Forschungsgemeinschaft. Lais Gimenes Vernasqui reports financial support was provided by State of São Paulo Research Foundation. Suelem Soares dos Santos reports financial support was provided by State of São Paulo Research Foundation. If there are other authors, they declare that they have no known competing financial interests or personal relationships that could have appeared to influence the work reported in this paper.

Acknowledgement

We would like to express our gratitude to Prof. Matthias Arenz from University of Bern for sharing the schematics of the half-cell setup and Lena Geiling from University of Bayreuth for technical support with SEM-EDX and XPS. The authors gratefully acknowledge the Chair of Inorganic Chemistry III – Prof. Dr. Jürgen Senker, as a member of the North Bavarian NMR Center (NBNC), and Beate Bejor (University of Bayreuth) for their valuable support and assistance with the solid-state

^{15}N NMR measurements. The SEM-EDX (Ultra Zeiss Plus) and XPS/UPS facility (PHI 5000 VersaProbe III system) at the Keylab Device Engineering in Bavarian Polymer Institute, University of Bayreuth is also acknowledged.

Part of this research was carried out at the experimental facilities at Petra III, DESY (Hamburg, Germany), a member of the Helmholtz Association HGF and we would like to thank Edmund Welter for the assistance provided while using the P65 beamline (beamtime was allocated for proposal I-20240745).

B.F.G. and C.R. acknowledge the financial support from the Federal Ministry of Research, Technology and Space (BMFTR) under the funding codes Real XAS (Grant 05K25WC1), Live XAS (Grant 05K22WC1) and HighHy (Grant 03SF0689B). P.H. also gratefully acknowledges additional support from the Deutsche Forschungsgemeinschaft (DFG, German Research Foundation) [529993860].

L.G.V., J.E.C and S.S.S. acknowledge the funding granted by the São Paulo Research Foundation, FAPESP, (grant numbers #2019/18572–7 #2024/06899–0, #2023/06233–9, #2022/07225–7, #2024/12856–1). The authors would like to express their gratitude to Dr. Michael Haumann and Prof. Holger Dau from Freie Universität Berlin for providing access to the SimXLite software (for EXAFS fit) developed by the scientists at the KMC-3 beamline at BESSY-HZB.

Supplementary materials

Supplementary material associated with this article can be found, in the online version, at doi:10.1016/j.electacta.2026.148958.

References

[1] Y. Chen, R. Wang, H. Du, Z. Yang, M. Cai, Y. Wang, Triphenylamine mediated strategy for high-stability polyaniline-based zinc ion battery, J. Power. Sources 659 (2025) 238406, https://doi.org/10.1016/j.jpowsour.2025.238406.

[2] Z. Liu, L. Chen, H. Wen, T. Zhang, J. Li, H. Yang, In-situ polymerized polyaniline-decorated V2C MXene nanosheets as a high-performance cathode material for aluminium-ion batteries, Electrochim. Acta 541 (2025) 147363, https://doi.org/10.1016/j.electacta.2025.147363.

[3] M. Alsaiari, A. Yasmeen, A.M. Afzal, M.W. Iqbal, J.S. Algethami, F.A. Harraz, Designing of poly(vinyl) alcohol and polyaniline conducting polymers doped WS2@rGO@AC hybrid nanocomposite electrode for high performance energy storage devices, Synth. Met. 307 (2024) 117649, https://doi.org/10.1016/j.synthmet.2024.117649.

[4] H. Abdollahi-Esfahlani, H. Sabzmeydani, S. Pourmahdian, A. Tanha, A. Hadjizadeh, Development of three-dimension polyaniline-based ternary hierarchical architectures as chemiresistive ammonia gas sensor and smart green label for fish freshness, Microchem. J. 217 (2025) 114845, https://doi.org/10.1016/j.microc.2025.114845.

[5] S. Chutia, K. Phukan, High-performance supercapacitor electrode from betel nut nanocellulose/polyaniline/ZnO ternary nano-composite, Next Mater. 10 (2026) 101359, https://doi.org/10.1016/j.nxmate.2025.101359.

[6] K. El Khammassi, M. Messali, A.A. Alrashdi, Y. El Aoufir, H. Lgaz, O. Benali, A. Sabik, H. Erramli, Innovative application of electro-polymerized polyaniline for enhanced corrosion protection of aluminum alloys in chloride environments, J. Mater. Res. Technol. 38 (2025) 2378–2391, https://doi.org/10.1016/j.jmrt.2025.08.071.

[7] S. Bhadra, D. Khastgir, N.K. Singha, J.H. Lee, Progress in preparation, processing and applications of polyaniline, Prog. Polym. Sci. 34 (8) (2009) 783–810, https://doi.org/10.1016/j.progpolymsci.2009.04.003.

[8] C.A. Escanio, S. S dos Santos, J. M Natale, D. A de L Almeida, V.J. Trava-Airoldi, E. J. Corat, Polyaniline–Lead composites as inhibitors for the hydrogen evolution reaction, relevant for lead-acid batteries, J. Phys. Chem. C 128 (13) (2024) 5490–5504, https://doi.org/10.1021/acs.jpcc.3c07481.

[9] S.-X. Wu, G.-R. Li, Recent progress in polyaniline-based catalysts for electrochemical energy conversion, Nanoscale 17 (27) (2025) 16114–16152, https://doi.org/10.1039/D5NR00966A.

[10] M. Yu, E. Budiyanto, H. Tüysüz, Principles of water electrolysis and recent progress in cobalt-, nickel-, and iron-based oxides for the oxygen evolution reaction, Angew. Chem. Int. Ed. 61 (1) (2022) e202103824, https://doi.org/10.1002/anie.202103824.

[11] C.C.L. McCrory, S. Jung, J.C. Peters, T.F. Jaramillo, Benchmarking heterogeneous electrocatalysts for the oxygen evolution reaction, J. Am. Chem. Soc. 135 (45) (2013) 16977–16987, https://doi.org/10.1021/ja407115p.

[12] A. Higareda, D.L. Hernández-Arellano, L.C. Ordoñez, R. Barbosa, N. Alonso-Vante, Advanced electrocatalysts for the oxygen evolution reaction: from single- to multielement materials, Catalysts. 13 (2023) 1346, https://doi.org/10.3390/catal13101346.

[13] J. Yuan, X. Cheng, C. Lei, B. Yang, Z. Li, K. Luo, K.H. Koko Lam, L. Lei, Y. Hou, K. K. Ostrikov, Bimetallic oxyhydroxide as a high-performance water oxidation electrocatalyst under industry-relevant conditions, Engineering 7 (9) (2021) 1306–1312, https://doi.org/10.1016/j.eng.2020.01.018.

[14] L. Chen, H. Tan, Y.-P. Zhang, K. Song, H. Liu, J.-J. Wang, Orthogonal control of lattice oxygen activation and oxygen evolution reaction suppression via "molecular gates" for high-efficiency nitrile electrosynthesis, Angew. Chem. Int. Ed. 64 (43) (2025) e202513640, https://doi.org/10.1002/anie.202513640.

[15] L.C. Seitz, C.F. Dickens, K. Nishio, Y. Hikita, J. Montoya, A. Doyle, C. Kirk, A. Vojvodic, H.Y. Hwang, J.K. Norskov, et al., A highly active and stable IrOx/SrIrO3 catalyst for the oxygen evolution reaction, Science (1979) 353 (6303) (2016) 1011–1014, https://doi.org/10.1126/science.aaf5050.

[16] H. Cheraparambil, M. Vega-Paredes, Y. Wang, H. Tüysüz, C. Scheu, C. Weidenthaler, Deciphering the role of Fe impurities in the electrolyte boosting the OER activity of LaNiO3, J. Mater. Chem. A 12 (9) (2024) 5194–5203, https://doi.org/10.1039/D3TA06733E, 10.1039/D3TA06733E.

[17] L. Twight, A. Tonsberg, S. Samira, K. Velinkar, K. Dumpert, Y. Ou, L. Wang, E. Nikolla, S.W. Boettcher, Trace Fe activates perovskite nickelate OER catalysts in alkaline media via redox-active surface Ni species formed during electrocatalysis, J. Catal. 432 (2024) 115443, https://doi.org/10.1016/j.jcat.2024.115443.

[18] I. Spanos, J. Masa, A. Zeradjanin, R. Schlögl, The effect of iron impurities on transition metal catalysts for the oxygen evolution reaction in alkaline environment: activity mediators or active sites? Catal Lett. 151 (7) (2021) 1843–1856, https://doi.org/10.1007/s10562-020-03478-4.

[19] D. Gutiérrez-Martín, A. Asserghine, A. Torres-Pardo, Á. Varela, J. Rodríguez-López, J.M. González-Calbet, M. Parras, Evaluating the impact of iron impurities in KOH on OER performance of BaNiO3 single crystals using scanning electrochemical cell microscopy, Electrochim. Acta 499 (2024) 144705, https://doi.org/10.1016/j.electacta.2024.144705.

[20] R.A. Márquez, K. Kawashima, Y.J. Son, G. Castelino, N. Miller, L.A. Smith, C. E. Chukwuneke, C.B. Mullins, Getting the basics right: preparing alkaline electrolytes for electrochemical applications, ACS Energy Lett. 8 (2) (2023) 1141–1146, https://doi.org/10.1021/acsenergylett.2c02847.

[21] K. Ramalingam, S. Panchu, A.S. Salunke, K. Muthukumar, A. Ramanujam, S. Muthiah, Free-standing graphene/conducting polymer hybrid cathodes as FTO and Pt-Free electrode for quasi-State dye sensitized solar cells, ChemistrySelect. 1 (15) (2016) 4814–4822, https://doi.org/10.1002/slct.201600874.

[22] A. Korent, K. Žagar Soderžnik, S. Šturm, K. Žužek Rožman, A correlative study of polyaniline electropolymerization and its electrochromic behavior, J. Electrochem. Soc. 167 (10) (2020) 106504, https://doi.org/10.1149/1945-7111/ab9929.

[23] A.Y. Obaid, E.H. El-Mossalamy, S.A. Al-Thabaiti, I.S. El-Hallag, A.A. Hermas, A. M. Asiri, Electrodeposition and characterization of polyaniline on stainless steel surface via cyclic, convolutive voltammetry and SEM in aqueous acidic solutions, Int. J. Electrochem. Sci. 9 (2) (2014) 1003–1015, https://doi.org/10.1016/S1452-3981(23)07773-8.

[24] I. Elghamry, A.S. Alablan, M.A. Alkhalifah, M.E. Abdelsalam, High-performance organometallic catalyst based on nickel porphyrin/carbon fibre for the oxygen reduction reaction, J. Electrochem. Soc. 168 (1) (2021) 016510, https://doi.org/10.1149/1945-7111/abd572.

[25] K.R. Prasad, N. Munichandraiah, Electrocatalytic efficiency of polyaniline by cyclic voltammetry and electrochemical impedance spectroscopy studies, Synth. Met. 126 (1) (2002) 61–68, https://doi.org/10.1016/S0379-6779(01)00496-9.

[26] V.A. Setyowati, L. Noerochim, D. Susanti, Y. Pradesar, H.-C. Huang, S.-T. Chang, K.-C. Wang, C.-H. Wang, High oxygen reduction reaction activity on various iron loading of Fe-PANI/C catalyst for PEM fuel cell, Ion (Kiel) 26 (2) (2020) 813–822, https://doi.org/10.1007/s11581-019-03240-w.

[27] A.F. Richter, A. Ray, K.V. Ramanathan, S.K. Manohar, G.T. Furst, S.J. Opella, A. G. MacDiarmid, A.J. Epstein, 15N NMR of polyaniline, Synth. Met. 29 (1) (1989) 243–249, https://doi.org/10.1016/0379-6779(89)90302-0.

[28] S. Kuroki, Y. Hosaka, C. Yamauchi, S. Nagata, M. Sonoda, 15N solid-state nuclear magnetic resonance study of pyrolyzed metal-polyaniline cathode catalysts for oxygen reduction in fuel cells, J. Power. Sources. 290 (2015) 8–13, https://doi.org/10.1016/j.jpowsour.2015.04.177.

[29] M.J. Rokosz, J.L. Gerlock, A.V. Kucherov, K.D. Belfield, N.L. Fryer, G. Moad, 15N CP/MAS solid-state NMR spectroscopy of a 15N-enriched hindered amine light stabilizer photolyzed in acrylic/melamine and acrylic/urethane coatings, Polym. Degrad. Stab. 70 (1) (2000) 81–88, https://doi.org/10.1016/S0141-3910(00)00092-6.

[30] Z.D. Zujovic, G.A. Bowmaker, H.D. Tran, R.B. Kaner, Solid-state NMR of polyaniline nanofibers, Synth. Met. 159 (7) (2009) 710–714, https://doi.org/10.1016/j.synthmet.2008.12.023.

[31] Z. Zujovic, P.A. Kilmartin, J. Travas-Sejdic, The applications of solid-State NMR to conducting polymers. The special case on polyaniline, Molecules. 25 (2020) 444, https://doi.org/10.3390/molecules25030444.

[32] A. Bekhoukh, I. Moulefera, L. Sabantina, A. Benyoucef, Development, investigation, and comparative study of the effects of various metal oxides on optical electrochemical properties using a doped PANI matrix, Polym. (Basel) 13 (2021) 3344, https://doi.org/10.3390/polym13193344.

[33] X. Wei, Z. Yin, K. Lyu, Z. Li, J. Gong, G. Wang, L. Xiao, J. Lu, Z. Lin, Highly selective reduction of CO2 to C2+ hydrocarbons at copper/polyaniline interfaces, ACS. Catal. 10 (2020) 4103–4111, https://doi.org/10.1021/acscatal.0c00049.

[34] G. Kowalski, J. Pielichowski, M. Grzesik, Characteristics of polyaniline cobalt supported catalysts for epoxidation reactions, Sci. World J. 2014 (1) (2014) 648949, https://doi.org/10.1155/2014/648949.

[35] E.T. Kang, K.G. Neoh, K.L. Tan, ESCA studies of protonation in Polyaniline, Polym. J. 21 (11) (1989) 873–881, https://doi.org/10.1295/polymj.21.873.

[36] X. Yin, H.T. Chung, U. Martinez, L. Lin, K. Artyushkova, P. Zelenay, PGM-free ORR catalysts designed by templating PANI-type polymers containing functional groups with high affinity to iron, J. Electrochem. Soc. 166 (7) (2019) F3240, https://doi.org/10.1149/2.0301907jes.
[37] C.M.S. Izumi, V.R.L. Constantino, A.M.C. Ferreira, M.L.A Temperini, Spectroscopic characterization of polyaniline doped with transition metal salts, Synth. Met. 156 (9) (2006) 654–663, https://doi.org/10.1016/j.synthmet.2005.12.023.
[38] C.M.S. Izumi, A.M.D.C. Ferreira, V.R.L. Constantino, M.L.A Temperini, Studies on the interaction of emeraldine base polyaniline with Cu(II), Fe(III), and Zn(II) ions in solutions and films, Macromolecules. 40 (9) (2007) 3204–3212, https://doi.org/10.1021/ma062905o.
[39] B. Shi, H. Li, X. Fu, C. Zhao, A.H. Wang, W. Tan, Y. Rao, M. Li, S. Komarneni, H. Yang, Insight into the key role of imine groups in polyaniline for adsorbing heavy metal ions: density functional theory and experimental study, Sep. Purif. Technol. 335 (2024) 125866, https://doi.org/10.1016/j.seppur.2023.125866.
[40] K.F. Qasim, M.A. Mousa, Physicochemical properties of oriented crystalline assembled polyaniline/metal doped Li4Ti5O12 composites for Li-ion storage, J. Inorg. Organomet. Polym. Mater. 33 (9) (2023) 2601–2617, https://doi.org/10.1007/s10904-023-02720-x.
[41] K. Artyushkova, Misconceptions in interpretation of nitrogen chemistry from x-ray photoelectron spectra, J. Vac. Sci. Technol. A 38 (3) (2020) 031002, https://doi.org/10.1116/1.5135923.
[42] Z. Morávková, I. Šeděnková, P. Bober, The first stages of chemical and electrochemical aniline oxidation—Spectroscopic comparative study, Appl. Sci. 10 (2020) 2091, https://doi.org/10.3390/app10062091.
[43] Y. Liu, D. Zhou, T. Deng, G. He, A. Chen, X. Sun, Y. Yang, P. Miao, Research progress of oxygen evolution reaction catalysts for electrochemical water splitting, ChemSusChem 14 (24) (2021) 5359–5383, https://doi.org/10.1002/cssc.202101898.
[44] H.M. Abo-Dief, Production of oxygen via water oxidation using PANI@CuMn2O4 nanocomposite electrocatalyst for OER, Mater. Chem. Phys. 326 (2024) 129803, https://doi.org/10.1016/j.matchemphys.2024.129803.
[45] X. Zou, Q. Lu, M. Tang, J. Wu, K. Zhang, W. Li, Y. Hu, X. Xu, X. Zhang, Z. Shao, et al., Catalyst–Support interaction in polyaniline-supported Ni3Fe oxide to boost oxygen evolution activities for rechargeable Zn-air batteries, Nano-Micro Lett. 17 (1) (2024) 6, https://doi.org/10.1007/s40820-024-01511-4.
[46] R. Djara, N. Masquelez, M.-A. Lacour, A. Merzouki, J. Cambedouzou, D. Cornu, S. Tingry, Y. Holade, Self-supported electrocatalysts derived from nickel-cobalt modified polyaniline polymer for H2-evolution and O2-evolution reactions, ChemCatChem 12 (22) (2020) 5789–5796, https://doi.org/10.1002/cctc.202001235.
[47] V. Ashok, S. Mathi, M. Sangamithirai, J. Jayabharathi, Regulated bimetal-doped polyaniline: amorphous-crumple-structured viable electrocatalyst for an efficient oxygen evolution reaction, Energy Fuels 36 (23) (2022) 14349–14360, https://doi.org/10.1021/acs.energyfuels.2c03022.
[48] Y. Zou, Y.-Z. Wu, Y. Huang, J.-L. Liu, H. Liu, J.-J. Wang, Engineering the electronic structure of Ni3FeS with polyaniline for enhanced electrocatalytic performance of overall water splitting, Nanotechnology 33 (44) (2022) 445701, https://doi.org/10.1088/1361-6528/ac83cb.
[49] Y. Zou, Y. Huang, L.-W. Jiang, A. Indra, Y. Wang, H. Liu, J.-J. Wang, Polyaniline coating enables electronic structure engineering in Fe3O4 to promote alkaline oxygen evolution reaction, Nanotechnology 33 (15) (2022) 155402, https://doi.org/10.1088/1361-6528/ac475c.
[50] X. Fan, Y. Ma, A. Sun, X. Zhang, L. Tang, J. Guo, Engineering heterogeneous nickel-iron oxide/iron phosphate on P, N co-doped carbon fibers for efficient oxygen evolution reaction in neutral and alkaline solutions, Surf. Interfaces 25 (2021) 101193, https://doi.org/10.1016/j.surfin.2021.101193.
[51] M. Mattinen, J. Schröder, G. D'Acunto, M. Ritala, T.F. Jaramillo, M.B. Stevens, S. F. Bent, Dynamics of precatalyst conversion and iron incorporation in nickel-based alkaline oxygen evolution reaction catalysts, Cell Rep. Phys. Sci. 5 (11) (2024) 102284, https://doi.org/10.1016/j.xcrp.2024.102284.